Low-Current-Density Magnetic Tunnel Junctions for STT-RAM Application Using MgO_xN_{1-x} ($x = 0.57$) Tunnel Barrier

Mohamad G. Moinuddin, Aijaz H. Lone, Shivangi Shringi, Srikant Srinivasan, *Member, IEEE*, and Satinder K. Sharma, *Member, IEEE*

***Abstract*—High switching speed, endurance, and low-current-based perpendicular magnetic tunnel junction (p-MTJ) memory is attracting wide interest as a key promising candidate for next-generation spintronic memory technology. p-MTJ-based spin-transfer torque RAM (STT-RAM) has been extensively investigated, and despite the promise, there is concern about the high switching current density and low stability with regard to scaling. In this work, the current controllability of p-MTJ in iron (Fe)-enriched $Co_{20}Fe_{60}B_{20}$ with a newly designed MgO_xN_{1-x} tunnel layer is systematically investigated, with the expectation that the introduction of N minimizes the oxidation of Fe to improve the performance of the device. A facile, plasma-based oxynitridation ($MgO_{x=0.57}N_{1-x=0.43}$) of MgO through RF-sputter deposition serves as a reliable procedure to establish a tunnel barrier for an MTJ structure fabricated with ~300-nm diameter and pinned with synthetic antiferromagnetic (SAF) $[Co/Pt]_n$ multilayer stack. Current-controlled tunneling magnetoresistance (TMR) up to ~65% was observed at room temperature (RT) with ultralow switching current density (J_c) of 136 ± 17 kA/cm^2. TMR along with tunnel conductance ($g(V)$) was measured to be highly stable in the read-bias regime (-200 to $+200$ mV) for MgO_xN_{1-x} as compared to the reported MgO barrier. The analogous MgO_xN_{1-x}-based MTJ structures were modeled using the nonequilibrium Green's function (NEGF) with appropriate tunnel barrier parameters and incorporating modulated barrier height as compared with the MgO barrier. The current–voltage characteristics of the modeled device showed close agreement with experimental data indicating high spin current. Based on the field-induced magnetization analysis, the macro-magnetic reversal analysis suggests the free-layer switching duration of ~3 ns. These observations show the strong candidature of MgO_xN_{1-x} ($x = 0.57$) MTJs for STT-RAM device application.**

***Index Terms*—Low current density, oxynitrides, perpendicular magnetic tunnel junction (p-MTJ), spintronics, tunnel barrier.**

Manuscript received September 10, 2019; revised November 4, 2019; accepted November 5, 2019. Date of publication December 17, 2019; date of current version December 30, 2019. The work of M. G. Moinuddin was supported by the Ministry of Electronics and Information Technology (MeitY), Government of India, through Visvesvaraya PhD Scheme. The review of this article was arranged by Editor G. L. Snider. *(Corresponding author: Satinder K. Sharma.)*

The authors are with the School of Computing and Electrical Engineering (SCEE), Indian Institute of Technology (IIT) Mandi, Mandi 175005, India (e-mail: srikant@iitmandi.ac.in; satinder@iitmandi.ac.in).

Color versions of one or more of the figures in this article are available online at http://ieeexplore.ieee.org.

Digital Object Identifier 10.1109/TED.2019.2954131

I. Introduction

MAGNETIC tunnel junction (MTJ)-based spintronic devices have gained huge attention due to their improved performance and broad panel of applications [1]–[3]. In particular, recent developments in MTJ-based devices have shown a path for futuristic low-power memory applications [4], [5]. In particular, the perpendicular MTJ (p-MTJ) with spin-transfer torque (STT)-based switching possesses nonvolatile behavior with high endurance, fast switching, and simple device structure [6], [7]. On the other hand, as the cell area is scaled down to meet density and power demands, conventional STT-RAM suffers from endurance and reliability issues due to the aging of the ultrathin tunnel barrier and read current disturbance [6]. Furthermore, there is an imperative need to lower STT switching current densities to further reduce power consumption that has still not yet been met [4], [8].

For stable ON/OFF ratio measured by tunneling magnetoresistance (TMR) with sufficient write/erase margin, the tunnel barrier must be 2.0 nm or less [5]. Hence, forming a high-quality tunnel barrier is a key factor in realizing a state-of-the-art MTJ with high thermal stability ($\Delta > 60$) for a 10-year data retention time and a low switching current density ($J_c \sim 1$ MA/cm^2). Numerous attempts have been made to fabricate p-MTJs using Al_2O_3, Ta_2O_5, Gd_2O_3, NiO, HfO_2, h-BN, and MgO as a tunnel barrier in the recent past [9]–[14]. In the series of materials tried as a tunnel barrier, MgO has proven to be the preferred because of the interface spin filtering property and also inherently a reasonable bandgap (7.5 eV) [15]. It is also found that the switching current density (10^6 A/cm^2) and anomalous TMR (negative TMR) are due to adjoining ferromagnetic impurity diffusion in MgO tunnel barriers which result in increased switching current and the terminal resistance [16].

In iron-enriched Heusler alloy ($Co_{20}Fe_{60}B_{20}$)-based MTJ, the increased Fe provides better spin polarization (67%) and perpendicular magnetic anisotropy (PMA). However, Fe diffusion into tunnel oxide barrier forms Fe-O and reduces the interface anisotropy of MTJ significantly [17]. Moreover, this diffused Fe acts as ferromagnetic impurity inside the tunnel barrier and further affects the TMR of the memory devices [18]. To overcome this issue of interlayer diffusion, oxynitrides (SiON, AlON, and TiON) have

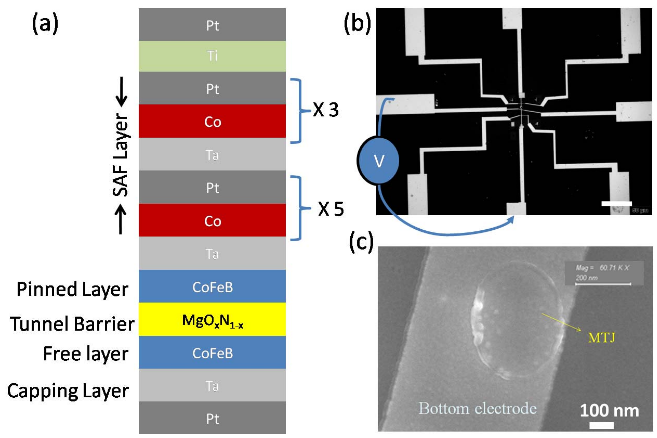

Fig. 1. MTJ, device geometry, and morphology. (a) Device layer stack consisting Pt/Ta/CoFeB/MgO_xN_{1-x}/CoFeB/Ta/SAF/Ti/Pt. (b) Top view of a vertical MTJ device by optical microscopy with scale bar 50 μm. (c) Nanoscopic morphology of ~300-nm patterned MTJ with scale bar 200 nm.

been used in different types of electronics devices such as MOS (1T-1C)-based RAM, FeRAM, and similarly for MTJs [19]–[21]. In earlier stages of MTJ development, TiON, AlON, and TiAlON have been used with reactive sputtering and reactive ion-beam deposition technique as reported by Wei *et al.* [22] and Zhang *et al.* [23]. However, the reported outcomes were not very encouraging, and it was observed that the TMR was found either low or anomalous due to barrier asymmetry.

In this study, we investigated systematically the MgO_xN_{1-x}-based ultrathin film as an alternate tunnel barrier for MTJ applications. The objective of nitrogen incorporation inside the ultrathin barrier is to increase the diffusion resistance and prevent the interface oxidation of FM layers. The current density (J_c) and TMR of the fabricated device were analyzed in the absence of an external magnetic field ($H_m = 0$). The fabricated and investigated p-MTJ showed promising values of J_c and TMR. The crystallinity, physical state, and tunnel barrier effective composition (Mg:O:N) were analyzed using various spectroscopic investigations.

II. Experiment

In order to investigate the current-induced switching (CIS) in the MgO_xN_{1-x}-based p-MTJ, a set of devices were fabricated as per the standard semiconductor processing, i.e., multistep lithography, thin-film MTJ stack deposition, annealing, and metallization [24]. The fabricated MTJ blanket was as follows: Ta/$[Co/Pt]_n$/Ta/$C_{20}Fe_{60}B_{20}$/MgO_xN_{1-x}/$C_{20}Fe_{60}B_{20}$/Ta/Pt/Ti/SiO_2/Si. As depicted in the schematic of Fig. 1(a), multilayer p-MTJ device structure consists of (all parenthesis values are in nm): Ta (5) seed layer; $Co_{20}Fe_{60}B_{20}$ (2) free layer (FL); MgO_xN_{1-x} (1.6) tunneling layer; $Co_{20}Fe_{60}B_{20}$ (2) reference layer (RL); and $[Co/Pt]_5$/Ta/$[Co/Pt]_3$ synthetic antiferromagnetic (SAF) pinning layer. A series of nanometric (400 × 300 nm^2) elliptical trenches were patterned in bilayer polymethyl methacrylate (PMMA) using electron beam lithography (EBL) over micropatterned bottom Pt electrode [25]. Apart from nanotrenches, variable dimension microtrenches (10 × 10 to 50 × 50 μm^2) were formed using optical lithography to analyze the scaling behavior. The whole MTJ blanket was deposited in the prepatterned trenches at room temperature (RT) and the constant base pressure of ~9.0 × 10^{-7} mbar. MgO_xN_{1-x} tunnel barrier was RF sputtered from 99.999% pure MgO target under different partial pressure and arc plasma combinations. A series of experiments were performed for the incorporation of nitrogen in the MgO ultrathin film. The best plasma concentration was found to be Ar:N_2:O_2:: 3:3:1 ratio (all the results provided in this article are related to this recipe).

Considering the slow rate for precise deposition, the vacuum pressure was kept at 4 × 10^{-3} mbar with a gas concentration in 45: 45:15 sccm. The μ-Raman spectroscopy (Horibal Lab RAM) was performed under ~633 nm (100%) illuminations to analyze the effect of nitrogen presence inside the MgO lattice. Further control samples MgO_xN_{1-x}/Si(100) were investigated using the X-ray photoelectron spectroscopy (XPS) (Thermo-Scientific) with monochromatic Al Kα source. The spectroscopic investigation for the deposited MgO_xN_{1-x} suggests the significant amount of nitrogen incorporation in the MgO matrix. To confirm the minimal effect of nitrogen on the tunnel barrier interface, wafer-scale surface uniformity has been analyzed using surface topography analysis (not shown here). Since uniformly deposited MgO_xN_{1-x} has a lower bandgap than MgO, the tunnel barrier exhibits lower resistivity. Therefore, a higher barrier thickness can be used to realize high TMR simultaneously with a low-resistance area product, also reported elsewhere [23]. This newly developed tunnel barrier was sandwiched between the FL and RL. Thereafter, the layers of $[Co/Pt]_n$ superlattice SAF were deposited through RF (Co) and dc (Pt) co-sputtering from 99.999% pure Co and Pt targets over the rotating substrate (rpm-10). The materials were deposited alternatively to achieve the composition of the superlattice structure. A standard lift-off process was performed for p-MTJ fabrication from the deposited blanket explained elsewhere [26].

After liftoff, the deposited MTJ structures were annealed at 650 K with the ramp of 40 K/min for 1 h in a vacuum of 10^{-6} mbar to crystallize the deposited layers [8]. This multilayer structure results in the magnetic coupling between SAF and $Co_{20}Fe_{60}B_{20}$ with Ta spacer, which is further enhanced after annealing the $Co_{20}Fe_{60}B_{20}$/MgO_xN_{1-x} system. The surface morphology of fabricated MTJ along with the control sample has been systematically investigated. Fig. 1(b) and (c) shows the optical/top-down HRSEM image of fabricated MTJ. The top Pt/Ta electrodes were formed for vertical p-MTJ conduction analysis. Shorting between the overhanging regions of the top and bottom electrodes was blocked with HfO_2 (~27 nm) interlayer dielectric with a leakage current of pA order [27]. The fabricated device has been analyzed electrically at RT using a Keithley 4200 SCS tool in the current sweep mode. The retention analysis has been performed under a constant voltage bias mode.

III. Modeling and Numerical Simulation

The effect of nitrogen incorporation on switching characteristics of the fabricated MTJ was analyzed by numerically simulating the device using effective mass tight-binding (EMTB) with non-equilibrium Green's function (NEGF) formalism. To determine the appropriate parameters to input to the model, the experimental data were first fit into the Simmons' equation (1) to find out the effect of nitrogen on tunnel barrier properties such as barrier height (ϕ_B)

$$I(V)=\alpha(t_{ox})\cdot\left\{\begin{array}{l}\left(\phi_B-\frac{V}{2}\right)\exp\left[-1.025\cdot\left(\phi_B-\frac{V}{2}\right)^{\frac{1}{2}}\cdot t_{ox}\right]\\-\left(\phi_B+\frac{V}{2}\right)\exp\left[-1.025\cdot\left(\phi_B+\frac{V}{2}\right)^{\frac{1}{2}}\cdot t_{ox}\right]\end{array}\right\} \tag{1}$$

where t_{ox}, ϕ_B, and $\alpha(t_{ox})$ are the barrier thickness (in angstrom), barrier height, and thickness-dependent parameter. From the 2-D fit of the data, we find that barrier height has reduced from 0.93 in the case of MgO to 0.705 eV for MgO_xN_{1-x}[28]. Further variation in the effective mass of an electron in tunnel barrier along with change in lattice parameter (a_{ox}) with nitrogen incorporation was also studied. Different charges and spin current components are computed using the NEGF formalism

$$G^R(E)=[(E+i\eta)-H-\Sigma_L-\Sigma_R]^{-1} \tag{2}$$

where G^R is the Green's function, E is the energy range of transport, H is the device Hamiltonian, and $\sum_{L,R}$ represents the self-energy matrices corresponding to the left and right electrode.

The other important matrices we need for current calculation are the broadening matrices due to left and right contacts

$$\Gamma_L=i\left(\sum\nolimits_L-\sum\nolimits_L^+\right) \tag{3}$$

$$\Gamma_R=i\left(\sum\nolimits_R-\sum\nolimits_R^+\right). \tag{4}$$

The density spectral function, from whose diagonal elements we can compute the local density of states (DOS) of the device, is given by

$$A_L(E)=G\Gamma_LG^+ \quad\text{and}\quad A_R(E)=G\Gamma_RG^+. \tag{5}$$

The electron correlation function $G^n=A_Lf_L+A_Rf_R$, whose diagonal elements give the local electron density. The charge and spin current are computed from (5), while summing the current from each transverse mode k_t

$$I_{C\sigma}=\text{trace}\left\{\sum_{k_t}C_\sigma\frac{i}{\hbar}\left\{\begin{array}{c}H_{k,k+1}G^n_{k+1,k}\\-G^n{}_{k,k+1}H_{k+1,k}\end{array}\right\}\right\}. \tag{6}$$

Further to study the magnetization dynamics of the fabricated device, we simulated the analogous device in the object-oriented micromagnetic framework (OOMMF) [29]. The parameters were adapted from the experimental $M-H$ analysis such as magnetization saturation ($M_s=369$ emu/cc) and anisotropy field ($H_k=400$ Oe) for p-MTJ system.

IV. Results and Discussion

A. Spin-Transfer Switching

Fig. 2 shows CIS of the fabricated Ta/[Co/Pt]$_5$/Ta/[Co/Pt]$_3$/Ta/$C_{20}Fe_{60}B_{20}$/MgO_xN_{1-x}/$Co_{20}Fe_{60}B_{20}$/Ta p-MTJs

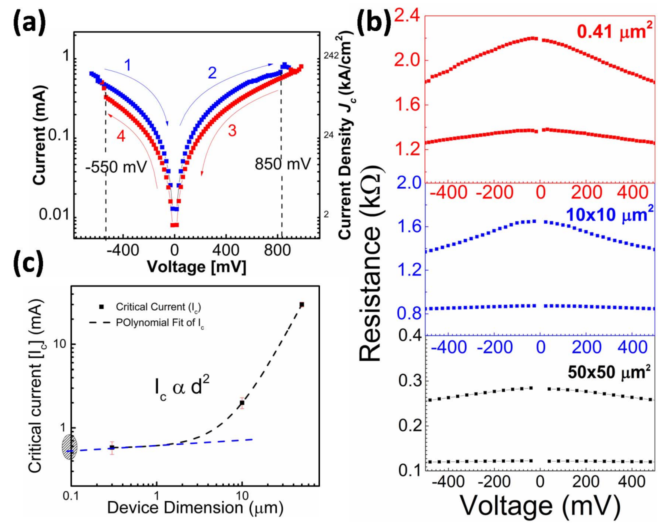

Fig. 2. Electrical switching of fabricated STT-RAM with MgO_xN_{1-x} tunnel barrier. (a) Current–voltage characteristics of the fabricated device. (b) TMR analysis for different device dimensions such as 300-nm, 10-μm, and 50-μm diameter. (c) Distribution of critical switching current as a function of the device area.

by dc two current-controlled electrical (CCE) characterization. While performing the cyclic $I-V$ characterization, the p-MTJ possesses different resistance states, i.e., parallel (P) and antiparallel (AP) states. P and AP states follow different current conduction paths 1→2→3→4→1 [as labeled in Fig. 2(a)]. As depicted in Fig. 2(a), the p-MTJ follows the high current path in the clockwise cycle 1→2 and get switch at +850 mV (i.e., 0.759 mA) from P to AP state. With further increase in bias, the device follows the AP path and after sweeping through the backward cycle to negative bias, and the device retains its AP state in 3→4 path up to −550 mV (i.e., −0.4016 mA). On the other hand, at −550 mV onward, the device gets its initial P state and repeats the 1→2→3→4→1 path. This bias-dependent asymmetric switching depicts the voltage asymmetry of STT on the FL [28]. Furthermore, it was observed that our results are in line with previously reported results for low-bias MTJ switching [30].

The computed average current densities (J_c) for P→AP and AP→P switching from the relation $Jc=(J_c^{P\to AP}+|J_c^{AP\to P}|)/(2)$, using the given values in Fig. 2(a), and found to be average current densities, $J_c=136\pm17$ kA/cm^2. This low current density value across the tunnel barrier is attributed to the nitrogen incorporation in the MgO barrier, which modulates the barrier height significantly along with the small reduction in interface anisotropy [30].

The TMRs of the fabricated MTJ structures were calculated from the R-V characteristics as shown in Fig. 2(b), using the two distinct resistance states. A TMR of ∼65% was achieved at zero bias for nanopillars p-MTJ and found to be symmetric across the read bias (±0.2 V). It is clearly shown in Fig. 2(b) that the device dimension does not alter the TMR due to PMA, whereas it requires more current to switch. The critical current (I_c) required for switching has been analyzed for different

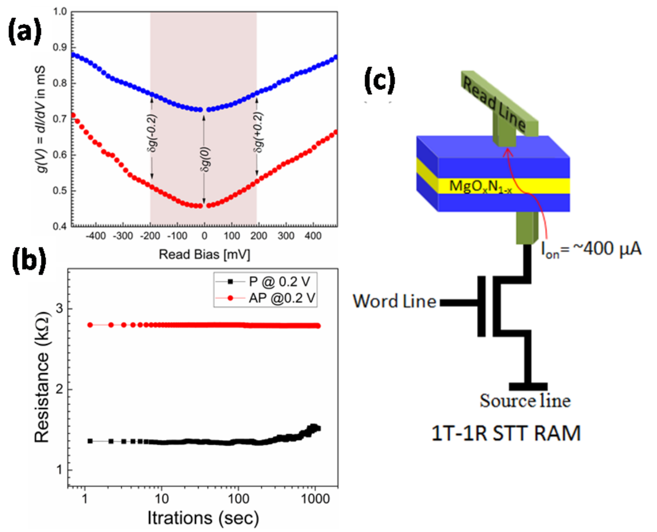

Fig. 3. (a) Tunneling conductance of MgO_xN_{1-x} barrier in STT-RAM. The difference δg P (blue) and AP conductance found in constant in the read-bias regime. (b) Data retention and stability analysis for 300-nm pillar p-MTJ. (c) Proposed schematic for 1T-1R geometry.

device diameters (d). Fig. 2(c) shows the critical current versus device dimension (I_c versus d) analysis for p-MTJ stack Ta/[Co/Pt]$_n$/Ta/$C_{20}Fe_{60}B_{20}$/MgO_xN_{1-x}/$C_{20}Fe_{60}B_{20}$/Ta/Pt/Ti/SiO_2/Si. It is clearly depicted that the critical current decreases as the polynomial function of the diameter reduction of the device; thus, the extrapolated I_c estimated to be a slow decay when the diameter of p-MTJ decreased below ~90 nm.

The measured current in P (I_P) and AP (I_{AP}) states at ±0.2 V were found to be ~160 and ~95 μA, which is line with the current across the bitline of frontline CMOS in 1T-1R configuration [as shown in Fig. 3(c)] [8], [34], [35]. Therefore, read current of the fabricated p-MTJ structure found much lesser than the write current, as desired, respectively, for the state-of-the-art stable device performance.

In addition, tunnel conductance $g(V) = I'(V)$ has been analyzed by numerically differentiating the I–V though the first-order derivative. Fig. 3(a) shows the nonlinear $g(V)$ across the bias, which suggests pure tunneling current conduction across the FM terminals. A small asymmetry can be seen in the negative and positive biases. This asymmetry could occur due to the difference in the quality of the interfaces shared by the tunnel barrier with the adjoining CoFeB layers, i.e., bottom CoFeB-MgO_xN_{1-x} and the top MgO_xN_{1-x}–CoFeB interfaces. Considering Simmons's approximation for tunneling conductance, the derived $g(V)$ fit well with a tunnel barrier thickness of 1.6 nm [36]. It was also observed that $\delta g(V)$ difference has been conserved at different read biases (−0.2, 0, and 0.2 V) and found 0.26 ± 0.02 mS. Thus, the existence of constant $g(V)$ value at a desirable read-bias regime suggests a stable device structure as nonvolatile memory. A data retention analysis for read bias of 0.2 V has been performed, and the resistance was found constant up to 1000 read iterations. Initially, the p-MTJ was kept in P state with biasing of −1 V followed by the retention analysis of P state resistance carried at 0.2 V. Similarly, p-MTJ was switched to AP state using write bias of 1 V and followed by the same retention analysis. Fig. 3(b) clearly shows the two distinct resistance states without the variation of resistances in P and AP states. The fabricated p-MTJ with low write current density operation provides higher reliability regarding data storage and higher retention in the fabricated p-MTJ structures.

Table I shows the comprehensive study of available reports related to oxynitrides and low J_c MTJ. It clearly perceives that MgON-based tunnel barrier shows good coordination between TMR and the state-of-the-art switching current density trade-off [37].

B. Effect of Nitrogen Incorporation on Transport and Magnetization Dynamics

Simmons' approximation for experimental electron transport analysis has obtained the best fit for barrier height (φ_B) 0.705 eV, which further justifies the hypothesis of barrier height modulation, as shown in Fig. 4(a) (ϕ_B for MgO is 0.93–1.1).

The reduction in effective barrier height may attribute to the generation of many energy levels in the bandgap of MgO, which effectively modulates the barrier height for tunneling [38]. We further used NEGF simulations to study the effect of N incorporation in tunnel barrier. Using an experiment-fit barrier height $\phi_B = 0.705$ eV, the simulation IV results are in close agreement with the experimental IV results, as shown in Fig. 4(b).

It is to be noted that small modifications in lattice parameter a_{MgON} (4.05 Å in a_{MgO} and 3.90 Å in a_{MgON}) and effective mass ($m_e*_{ox} = 0.18\ m_e$ in MgO and $0.17 m_e$ in MgO_xN_{1-x}) were done to match the experimental results, where m_e is the mass of an electron. As shown in Fig. 4(c) at the FL interface, it showed an increasing behavior of spin current with lowering barrier height in the case of MgO_xN_{1-x}. From 2-D surface, the plot shows that for the same bias point, the spin current is around five times more for MgO_xN_{1-x} than MgO, which reflects in the increased STT on FL magnetization and, hence, reduces the critical switching current as observed in the experiment.

The deposited p-MTJ blankets were investigated under the variable magnetic field to analyze the switching of FL and RL. Fig. 5(a) depicts that the fabricated p-MTJ consists of FL, RL, and SAF with perpendicular easy axes as the in-plane field switching has shown the absence of any discreet change in magnetization (shown in red), whereas the out-of-plane has clearly shown the discrete switching field for FL and RL. Furthermore, the switching of FL and RL was clearly observed by analyzing the magnetic susceptibility ($\chi = dM/dH$) under variable H-field. Possible p-MTJ flipping configurations have been depicted with up and down arrows, explaining the magnetization associated with the FL (small arrow) and RL (big arrow), as shown in the inset of Fig. 5(a). The calculated anisotropy field (H_k) is an important metric for the realization of a thermally stable magnetization state for out-of-plane easy axis p-MTJ. The H_k found 450 Oe

TABLE I
COMPARISON AND SUMMARY OF MgON-BASED STT-RAM

MTJ stack structure (Thickness in Å)	Tunnel barrier layer	*Jc* MA/cm^2	Thermal Stability Δ	Switching phenomena	TMR (%)	Reference
Ta(30)/Pt(100)/$[Co(6)/Pt(18)]_4$/Co(7)/ AlO_x/$[Co(7)/Pt(18)]_2$/Pt(32)	AlO_x	-	-	SMTE	15	Park *et al.* [31]
Ta (50)/NiFe (60)/MnFe(100)/NiFe (120)/AlON/NiFe (80)/Ta(5)	AlON	10	-	FIS	18	Sharma *et al.* [21]
CoFeB(15)/MgO(10)/CoFeB(11) /Ta(04)/Co(05)/[Co/Pt](40)/ Ru(8.5)/ Co(05)/ [Co/Pt](65)	MgO	2	-	SMTE	100	*Jyotirmoy et. al* [32]
Ir(0.48)/Co(0.5)/Mo(0.3)/CoFeB(0.8)/MgO(0.8)/CoFeB(0.8)/ Mo(0.3)/CoFeB(0.8)/MgO(0.6)	MgO		53	FIS (600 Oe)	210	Huai *et al.* [10]
Ta (50)/Ru(300)/Ta (50)/ NiFe(50)/$Ir_{22}Mn_78$ (100)/$Co_{90}Fe_{10}$(25)/Ru(09)/$Co_{20}Fe_{60}B_{20}$ (30) /MgO (24)/CoFeB (30)/Ta (50)/Ru(50)	MgO	-	-	FIS	190	Chen *et al.* [24]
W(40)/Fe(06)/MgO(10)CoFeB(10)/W(04)/Fe-CoFeB (14) MgO(11.5)/CoFeB(10.5)/W(2.4)/Co(04)/[Co/Pt]/Co(06)/Pt(03)/ Ru(03)/$[Co/Pt]_{n+3}$/Pt(30)/Ta(50)	MgO	9.17	38	FIS ±300 Oe	154	Lee *et al.* [17]
Ta (150)/Co20Fe60B20 (10)/MgO(8.4)/ Co20Fe60B20 (12)/Ta (50)/Ru(30)	MgO	0.0093	9.2±1.6	STT	20	Christian *et al.* [30]
Ta/ IrMn/CoFe/MgOxNy/CoFe/[Co/Ni]/Ru/ [Co/Ni]/CoFeB/Co (estimated from Patent)	MgON	-	-	STT	>70	Zhang *etal.* [23]
CoFeB(10)/MgO(10)/CoFeB(15)/[Co/ Pt](50)/Ru(8.5)/ [Co/Pt](100)/ Ru(50)	MgO	0.94	100	Field induced STT-SOT	35	A. Fert *et al.* [33]
Ta(50)/$[Co/Pt]_3$/Ta/$[Co/Pt]_5$(130)/Ta(12)/CoFeB(20)/MgON(16)/ CoFeB(20)/Ta(50)	**MgON**	**0.136**	**40**	**STT**	**65**	**This work**

Abbreviations: *SMTE- Spin Momentum transfer effect, SOT- Spin Orbital Torque effect, STT- Spin Transfer Torque effect*

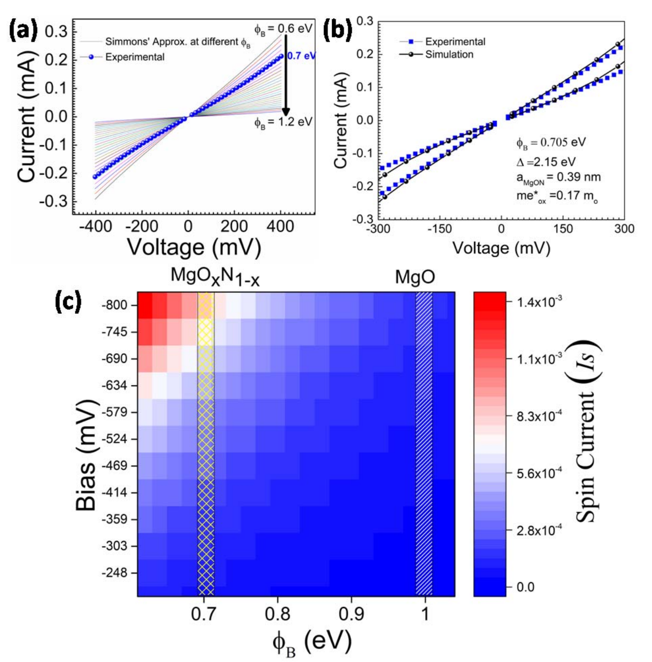

Fig. 4. Quantum transport analysis. (a) Simmons' approximation for quantum transport across the tunnel barrier; the experimental data matched well for φ_B value of 0.705 eV. (b) Comparison of *I–V* characteristics of p-MTJ with NEGF; both experimental and modeled data show a close agreement. (c) Effect of barrier height on the spin current at variable bias.

for saturation magnetization (M_s) 369.72 emu/cc. The thermal stability factor (Δ) has been calculated with H_k measured from field-induced switching analysis ($M - H$ curve). The thermal stability (Δ) of a p-MTJ has been explained as follows:

$$\Delta = \frac{E_b}{k_B T} = \frac{\mu_o M_s \cdot H_K V}{2k_B T} \tag{7}$$

where E_b, M_S,$k_{B,}$ V, and T are the energy barrier, saturation magnetization, Boltzmann's constant, FL volume, and temperature, respectively. The calculated Δ at RT found ∼40. The fabricated device with Δ = ∼40 is found stable in terms of current density/thermal stability tradeoff [33].

Fig. 5(b) depicts the FL magnetization reversal simulation in the presence of spin current for stack geometry analogous 300-nm nanopillar p-MTJ. Initially, reversal begins at the outer edges, and after 1 ns, as observed from Fig. 5(b), the domain formation and reversal take place. This nonuniform switching by domain reversal mechanism is also reflected in Fig. 5(a) $M - H$ curve. Further from the experimental $M - H$ curve, we observe that H_k has reduced slightly. Thus, the increased spin torque on FL, domain nucleation and reversal-based switching, and a small reduction in interface anisotropy appears to have reduced the switching current by many folds.

C. Realization of Oxynitride in Tunnel Barriers

To clarify the physical and chemical existence and quality of tunnel barrier, μ-Raman analyses of deposited MgO_xN_{1-x} and control samples were performed. Fig. 6(a) shows the

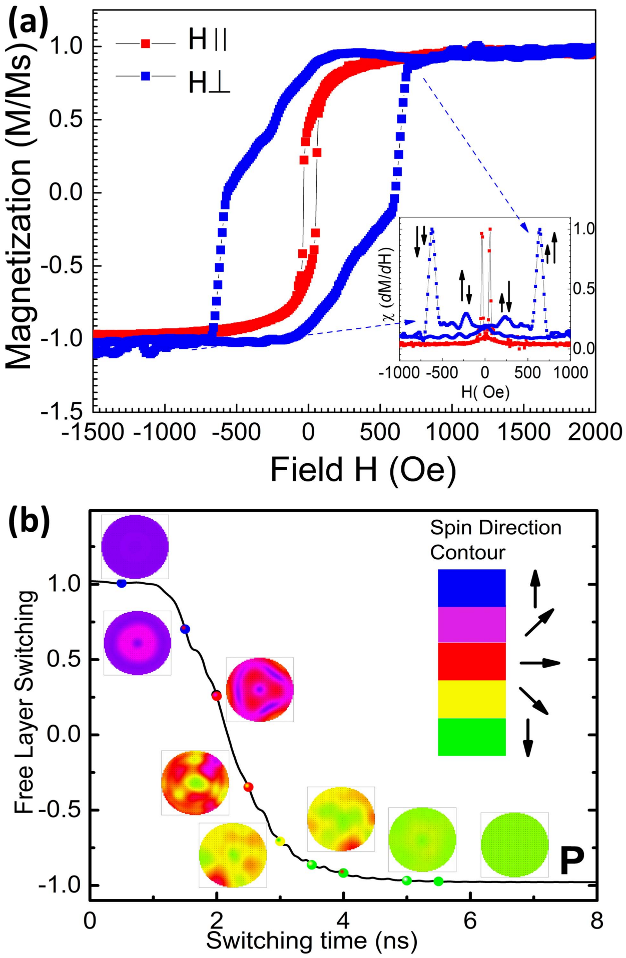

Fig. 5. Field-induced magnetization switching. (a) Magnetic field-induced switching analysis: the $M-H$ curve of the p-MTJ blanket with in-plane (H||) and out-of-plane (H⊥) field, change in susceptibility shows switching of the free and fixed layer at different fields (inset). (b) FL switching dynamics for 300-nm p-MTJ using OOMMF.

cumulative spectra for MgO_xN_{1-x} and MgO ultrathin films with MgO (100) substrate [39].The deposited films showed a broadened peak, which suggests the nanocrystallinity of the film in comparison with the crystalline MgO substrate [40]. The nitrogen substitution inside the MgO film provided a significant blue shift ($\Delta f - 20$ cm^{-1}), as shown in Fig. 6(b). These shifts may be attributed to N and Mg interaction, which results in bond length contraction. No peak broadening was observed in MgO_xN_{1-x}, with reference to MgO, after the nitrogen incorporation/substitution inside MgO. This suggests similar crystalline behavior as MgO [Fig. 6(b)]. Fig. 6(c) depicts the same trend in a shift at higher orders (1900 cm^{-1}) also. These blue shifts can also be explained as strain-induced inside the local crystal structure after lattice symmetry breaks due to nitrogen incorporation. This strain inside the film has provided a path to decrease the terminal resistance, which is as desired. Chen *et al.* [24] have shown that the effect of external strain on magnetization state and TMR of MTJ is minimal, and Kuczynski [41] has shown lowered resistivity of metal and metal alloy under strain condition. The chemical stability of MgO_xN_{1-x} film was analyzed using the XPS analysis. Fig. 6(d)–(f) shows the core/valence spectrum of magnesium,

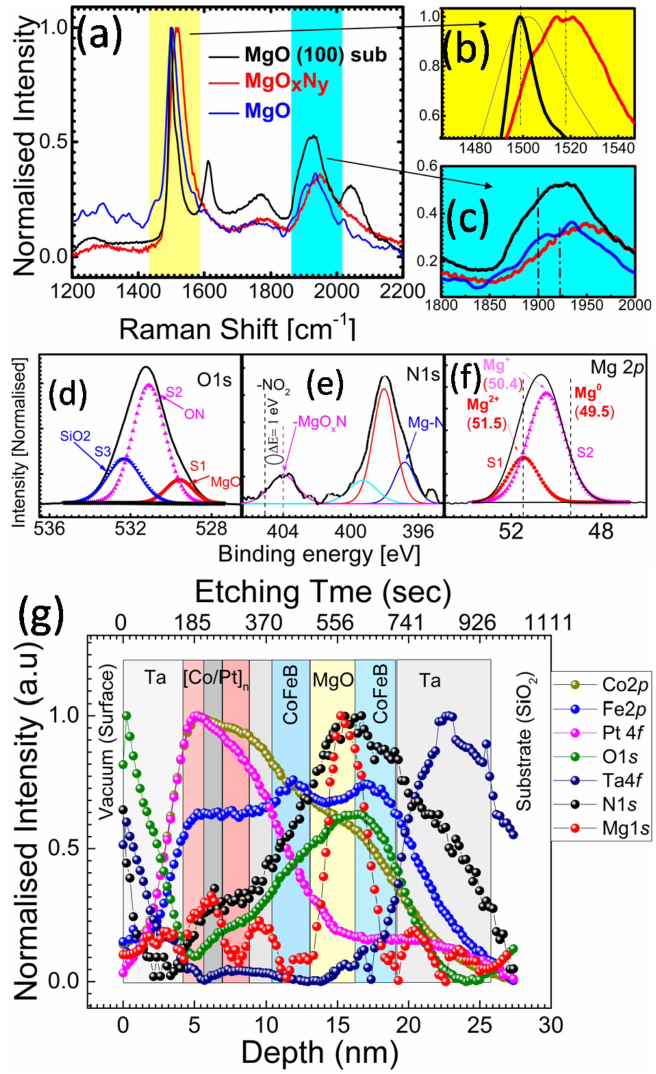

Fig. 6. Spectroscopic investigation of deposited tunnel barrier as a control sample. (a) Raman spectra of deposited MgO_xN_{1-x} deposited over Si(100) wafer; Si wafer was adapted due to significant difference between active mode spectra between thin film and substrate; we also compared with deposited MgO/Si and bare MgO (100) substrate, zoomed-in view (b) first-order and (c) higher-order Raman active mode of MgO and nitrogen substituted MgO. The XPS analysis shows (d) oxygen 1*s* core spectra and (e) nitrogen 1*s* core spectra; Mg chemical state analyzed by (f) valence band 2*p* spectra along with (g) XPS depth profile of the fabricated p-MTJ at 500-eV Ar^+ ion plasma.

oxygen, and nitrogen. The O 1*s* spectrum, as shown in Fig. 6(d), indicates the coexistence of –ON (531.11 eV) in the majority and -O- (529.60 eV) in the minority inside the film. On the other hand, the detected *N* 1*s* spectrum shows a similar existence of bonding of O = N– (398.2 eV) and –$O_{1+x}N$ (404 eV), as shown in Fig. 6(e). Furthermore, a small peak of Mg–N also found with fitted spectra suggests the formation of monolayer nitride which acts as the FM diffusion barrier as observed by Di Filippo *et al.* [42] for nitrogen insertion in Mg.

To further understand the tunnel junction, Mg 2*p* valence spectra were analyzed along with the KLL auger spectrum. Fig. 6(f) shows the fitted Mg^{2+}(51.5 eV) and Mg^+ (50.4 eV) with different areas and peak broadening full-width

TABLE II
RELATIVE CHEMICAL STATE OF THE MgON THIN FILM

Chem state	Peak Position (eV)	Areal density	FWHM	Relative concentration
Mg^{2+}	51.45244	17524.9872	1.61771	1
Mg^{+}	50.44218	51593.56565	1.95733	2.95

at half-maximum (FWHM). All the parameters are tabulated in Table II.

The metallic alloy contributes to the sharp peak, whereas insulators show peak broadening due to the charge accumulation on the surface. Furthermore, these spectra were fit using areal density to find the stoichiometric ratio of Mg:O:N. The deposition process uses single-crystal MgO (99.999%) bulk-source, so the Mg^{2+} shows the actual contribution of MgO, whereas Mg^{+} shows the reacted MgO with N_2 plasma. These ratios suggest MgO: MgON to be 1:2.95, as mentioned in Table II. The overall tunnel barrier could be $MgO_{0.57}N_{0.43}$. To realize the oxynitride tunnel barrier inside the p-MTJ stack, elementary depth profile analysis has been carried out in low-power (500 eV) Ar^{+} plasma. The elementary trace analyses were done after each etching with the data collection resolution <3 nm depth. Fig. 6(g) clearly depicts the normalized trace of elements over the approximated device thickness and found the availability of –ON inside the tunnel barrier.

V. CONCLUSION

In summary, a MgO_xN_{1-x} ($x = 0.57$) tunnel barrier was successfully deposited and incorporated into a $Co_{20}Fe_{60}B_{20}$/$MgO_{0.57}N_{0.43}$/$Co_{20}Fe_{60}B_{20}$ p-MTJ to investigate improvements in switching current over existing MgO-based p-MTJs. This tunnel barrier coupled with $Co_{20}Fe_{60}B_{20}$FL/RL has shown low switching current density (J_c) of 136 ± 17 kA/cm^2 across devices. Since the major hurdle to scaling STT-RAM has been the operating current density, this experiment demonstrates a pathway to low critical current density using tertiary oxynitride tunnel barrier with low resistance. Theoretical simulations using quantum transport and micromagnetics agree well with the experiment and suggest that the low current may be due to a reduction in barrier height and complexities of domain nucleation and reversal. Furthermore, the experimentally obtained TMR of $\sim$65%, in conjunction with the low switching current density, can be beneficial as it allows the use of the p-MTJ structure as is within the backend of the frontline CMOS processing. The enhanced barrier quality due to the incorporation of *N* decreases the aging effect, thus increasing data retention.

ACKNOWLEDGMENT

The authors would like to thank the Centre for Design and Fabrication of Electronic Devices (C4DFED), IIT Mandi, Mandi, India, and the Advanced Material Research Centre (AMRC), IIT Mandi, for the use of various state-of-the-art device fabrication and characterization facilities for this work.

REFERENCES

[1] A. Hirohata *et al.*, "Roadmap for emerging materials for spintronic device applications," *IEEE Trans. Magn.*, vol. 51, no. 10, Oct. 2015, Art. no. 0800511.

[2] G. Hu, T. Topuria, P. M. Rice, J. Jordan-Sweet, and D. C. Worledge, "Optimization of tunneling magnetoresistance in perpendicular magnetic tunnel junctions with Co|Pd reference layers," *IEEE Magn. Lett.*, vol. 4, 2013, Art. no. 3000104.

[3] J.-Y. Choi, D.-G. Lee, J.-U. Baek, and J. G. Park, "Double MgO-based perpendicular magnetic-tunnel-junction spin-valve structure with a top $Co_2Fe_6B_2$ free layer using a single SyAF [Co/Pt]$_n$ layer," *Sci. Rep.*, vol. 8, no. 1, 2018, Art. no. 2139.

[4] "International roadmap for devices and systems (IRDS) 2017 edition," IEEE Rep., 2017.

[5] A. Chen, "A review of emerging non-volatile memory (NVM) technologies and applications," *Solid-State Electron.*, vol. 125, pp. 25–38, Nov. 2016.

[6] J. J. Kan *et al.*, "A study on practically unlimited endurance of STT-MRAM," *IEEE Trans. Electron Devices*, vol. 64, no. 9, pp. 3639–3646, Sep. 2017.

[7] Z. Diao *et al.*, "Spin-transfer torque switching in magnetic tunnel junctions and spin-transfer torque random access memory," *J. Phys., Condens. Matter*, vol. 19, no. 16, 2007, Art. no. 165209.

[8] T. Endoh and H. Honjo, "A recent progress of spintronics devices for integrated circuit applications," *J. Low Power Electron. Appl.*, vol. 8, no. 4, p. 44, 2018.

[9] Y.-T. Chen, S. U. Jen, Y. D. Yao, and S. R. Jian, "Magnetostriction and tunneling magnetoresistance of Co/AlO_x/Co/IrMn junctions," *IEEE Trans. Magn.*, vol. 44, no. 11, pp. 2592–2594, Nov. 2008.

[10] Y. Huai *et al.*, "High performance perpendicular magnetic tunnel junction with Co/Ir interfacial anisotropy for embedded and standalone STT-MRAM applications," *Appl. Phys. Lett.*, vol. 112, no. 9, 2018, Art. no. 092402.

[11] C. L. Platt, B. Dieny, and A. E. Berkowitz, "Spin-dependent tunneling in HfO_2 tunnel junctions," *Appl. Phys. Lett.*, vol. 69, no. 15, 1996, Art. no. 2291.

[12] S. K. Arora, R. G. S. Sofin, and I. V. Shvets, "Magnetoresistance enhancement in epitaxial magnetite films grown on vicinal substrates," *Phys. Rev. B, Condens. Matter*, vol. 72, no. 13, 2005, Art. no. 134404.

[13] W. T. Sheng *et al.*, "Probing tunnel barrier shape and its effects on inversed tunneling magnetoresistance at high bias," *J. Electron. Mater.*, vol. 33, no. 11, pp. 1274–1279, 2004.

[14] M. Piquemal-Banci *et al.*, "2D-MTJs: Introducing 2D materials in magnetic tunnel junctions," *J. Phys. D, Appl. Phys.*, vol. 50, no. 20, 2017, Art. no. 203002.

[15] S. Ikeda *et al.*, "A perpendicular-anisotropy CoFeB-MgO magnetic tunnel junction," *Nature Mater.*, vol. 9, no. 9, pp. 721–724, Jul. 2010.

[16] A. Kalitsov *et al.*, "Bias dependence of tunneling magnetoresistance in magnetic tunnel junctions with asymmetric barriers," *J. Phys., Condens. Matter*, vol. 25, no. 49, 2013, Art. no. 496005.

[17] S.-E. Lee, J.-U. Baek, and J.-G. Park, "Highly enhanced TMR ratio and Δ for double MgO-based p-MTJ spin-valves with top $Co_2Fe_6B_2$ free layer by nanoscale-thick iron diffusion-barrier," *Sci. Rep.*, vol. 7, no. 17, 2017, Art. no. 11907.

[18] A. Filatov, A. Pogorelov, and Y. Pogoryelov, "Negative differential resistance in magnetic tunnel junction systems," *Phys. Status Solidi*, vol. 251, no. 1, pp. 172–177, Jan. 2014.

[19] R. Degraeve *et al.*, "Reliability prediction of direct tunneling RAM with SiON and HfSiON tunnel dielectrics based on transistor leakage current measurements," in *Proc. IEEE Int. Rel. Phys. Symp.*, no. 1, Mar. 2006, pp. 427–432.

[20] R. Khosla, D. K. Sharma, K. Mondal, and S. K. Sharma, "Effect of electrical stress on Au/Pb ($Zr_{0.52}$ $Ti_{0.48}$) O_3 /TiO_x N_y /Si gate stack for reliability analysis of ferroelectric field effect transistors," *Appl. Phys. Lett.*, vol. 105, no. 15, 2014, Art. no. 152907.

[21] M. Sharma, J. H. Nickel, T. C. Anthony, and S. X. Wang, "Spin-dependent tunneling junctions with AlN and AlON barriers," *Appl. Phys. Lett.*, vol. 77, no. 14, pp. 2219–2221, 2000.

[22] P. Wei *et al.*, "Composition analysis of the insulating barrier in magnetic tunnel junctions by grazing angle of incidence RBS," *Nucl. Instrum. Methods Phys. Res. B, Beam Interact. Mater. Atoms*, vol. 190, nos. 1–4, pp. 684–688, May 2002.

[23] K. Zhang, H.-C. Wang, M. Li, and J. Quan, "Magnetic read head with magnetoresistive (MR) enhancements toward low resistance X area (RA) product," U.S Patent 9 601 137 B2, Mar. 21, 2017.

[24] J.-Y. Chen, Y.-C. Lau, J. M. D. Coey, M. Li, and J.-P. Wang, "High performance MgO-barrier magnetic tunnel junctions for flexible and wearable spintronic applications," *Sci. Rep.*, vol. 7, Jan. 2017, Art. no. 42001.

[25] MicroChem. (2001). *NANO PMMA and Copolymer*. Accessed: Nov. 3, 2019. [Online]. Available: http://microchem.com/products/images/uploads/PMMA_Data_Sheet.pdf
[26] *MicroChemicals-Fundamentals of Microstructuring LIFT-OFF*. Accessed: Nov. 3, 2019. [Online]. Available: http://www.microchemicals.com/downloads/application_notes.html
[27] S. Sharma, S. Das, R. Khosla, H. Shrimali, and S. K. Sharma, "Realization and performance analysis of facile-processed μ-IDE-based multilayer HfS_2/HfO_2 transistors," *IEEE Trans. Electron Devices*, vol. 66, no. 7, pp. 3236–3241, Jul. 2019.
[28] D. Datta, B. Behin-Aein, S. Datta, and S. Salahuddin, "Voltage asymmetry of spin-transfer torques," *IEEE Trans. Nanotechnol.*, vol. 11, no. 2, pp. 261–272, Mar. 2012.
[29] *OOMMF Project at NIST*. Accessed: Nov. 2, 2019. [Online]. Available: https://math.nist.gov/oommf/
[30] J. C. Leutenantsmeyer *et al.*, "Spin-transfer torque switching at ultra low current densities," *Mater. Trans.*, vol. 56, no. 9, pp. 1323–1326, 2015.
[31] J.-H. Park, C. Park, T. Jeong, M. T. Moneck, N. T. Nufer, and J.-G. Zhu, "Co/Pt multilayer based magnetic tunnel junctions using perpendicular magnetic anisotropy," *J. Appl. Phys.*, vol. 103, no. 7, 2008, Art. no. 07A917.
[32] J. Chatterjee, T. Tahmasebi, J. Swerts, G. S. Kar, and J. De Boeck, "Impact of seed layer on post-annealing behavior of transport and magnetic properties of Co/Pt multilayer-based bottom-pinned perpendicular magnetic tunnel junctions," *Appl. Phys. Express*, vol. 8, no. 6, 2015, Art. no. 63002.
[33] J. Kan *et al.*, "Field-free switching of a perpendicular magnetic tunnel junction through the interplay of spin–orbit and spin-transfer torques," *Nature Electron.*, vol. 1, no. 11, pp. 582–588, Nov. 2018.
[34] *ONC18: 0.18 μm Process Technology*. Accessed: Sep. 8, 2019. [Online]. Available: https://www.onsemi.com/PowerSolutions/content.do?id=16678
[35] A. Driskill-Smith *et al.*, "Latest advances and roadmap for in-plane and perpendicular STT-RAM," in *Proc. 3rd IEEE Int. Mem. Workshop (IMW)*, May 2011, vol. 1, no. 408, pp. 1–3.
[36] J. G. Simmons, "Generalized formula for the electric tunnel effect between similar electrodes separated by a thin insulating film," *J. Appl. Phys.*, vol. 34, pp. 1793–1802, Jun. 1963.
[37] K. C. Chun, H. Zhao, J. D. Harms, T.-H. Kim, J.-P. Wang, and C. H. Kim, "A scaling roadmap and performance evaluation of in-plane and perpendicular MTJ based STT-MRAMs for high-density cache memory," *IEEE J. Solid-State Circuits*, vol. 48, no. 2, pp. 598–610, Feb. 2013.
[38] M. Pesci, F. Gallino, C. Di Valentin, and G. Pacchioni, "Nature of defect states in nitrogen-doped MgO," *J. Phys. Chem. C*, vol. 114, no. 2, pp. 1350–1356, 2010.
[39] Sigma-Aldrich. (2019). *Magnesium Oxide (Single Crystal Substrate), $\geq$99.9% Trace Metals Basis, <100>, L $\times$ W $\times$ Thickness 10 mm $\times$ 10 mm $\times$ 0.5 mm*. Accessed: Sep. 1, 2019. [Online]. Available: https://www.sigmaaldrich.com/catalog/product/aldrich/634646?lang=en&region=IN
[40] E. Ozkan, S.-H. Lee, C. E. Tracy, J. R. Pitts, and S. K. Deb, "Comparison of electrochromic amorphous and crystalline tungsten oxide films," *Sol. Energy Mater. Sol. Cells*, vol. 79, pp. 439–448, Sep. 2003.
[41] G. C. Kuczynski, "Effect of elastic strain on the electrical resistance of metals," *Phys. Rev.*, vol. 94, no. 1, pp. 61–64, 1954.
[42] G. Di Filippo, A. Classen, R. Pöschel, and T. Fauster, "Interaction of free-base tetraphenylporphyrin with magnesium oxide: Influence of MgO morphology on metalation," *J. Chem. Phys.*, vol. 146, no. 6, 2017, Art. no. 064702.